Effect of the temperature and HCl partial pressure on selective-area gas etching of (001) β-Ga_2O_3

Yuichi Oshima* and Takayoshi Oshima

Research Center for Electronic and Optical Materials, National Institute for Materials Science, Tsukuba, Ibaraki 305-0044, Japan

E-mail: OSHIMA.Yuichi@nims.go.jp

Abstract

We investigated the anisotropic selective-area HCl-gas etching behavior of SiO_2-masked (001) β-Ga_2O_3 and its dependence on the temperature T (548–949 °C) and HCl partial pressure P_0(HCl) (25–250 Pa). The cross-sectional width-to-depth aspect ratio of the etched trenches formed under the striped window along [010] decreased with increasing T and decreasing P_0(HCl). Secondary-ion mass spectrometry revealed slight diffusion of Si into β-Ga_2O_3 at T = 949 °C, while no diffusion was detected at T = 750 °C. These results provide practical guidelines for the fabrication of desired three-dimensional structures, such as fins/trenches, for high-performance β-Ga_2O_3-based power devices.

Monoclinic-structured β-Ga_2O_3 is an ultra-wide bandgap semiconductor, and it is promising for future power device applications. In addition to the large bandgap energy of 4.5–4.9 eV,[1,2)] melt-grown high-quality β-Ga_2O_3 single crystal substrates are

available[3-9] to grow high-quality homo/heteroepitaxial layers, which are essential for high-performance power devices, such as Schottky barrier diodes (SBDs),[10-13] modulation-doped FETs,[14,15] and MOS FETs (MOSFETs).[16-20]

To further increase the breakdown voltage of SBDs and enable normally-off operation of MOSFETs, introduction of three-dimensional (3D) structures, such as trench MOS SBDs[12,13] and fin FETs,[18,19] respectively, have been proven to be effective.

Such 3D structures have been mostly fabricated by reactive ion etching.[21] However, plasma damage is introduced on the processed surface and deteriorates the device performance.[22-24] Therefore, an alternative plasma-free dry etching technique is required. Accordingly, various plasma-free etching techniques have been investigated.[25-29] We recently demonstrated the selective HCl-gas etching technique and fabrication of fins/trenches along [010] with stable (100) sidewalls on a (001) β-Ga_2O_3 substrate,[29] which is particularly important for industrial use owing to the scalability and capability of the rapid growth of a high-quality epilayer.

The HCl-gas etching needs to be precisely controlled for practical device fabrication. Accordingly, in this study, we systematically investigated the effect of the temperature T and HCl partial pressure P_0(HCl) on the selective etching behavior of SiO_2-masked (001) β-Ga_2O_3 to obtain guidelines for practical device fabrication.

We used (001) β-Ga_2O_3 substrates (Novel Crystal Technology, Inc.) with a 0.1-μm-thick patterned SiO_2 mask for the etching experiments. The mask pattern included square windows (100 μm × 100 μm), circular windows with a diameter of 1.7 μm, and striped windows along [010] with a width of 1.4 μm. The SiO_2 film was deposited by plasma-assisted CVD using tetraethoxysilane as the precursor at 350 °C for 5.5 min. Conventional photolithography was used for patterning (see Ref. 30 for details).

The etching experiments were performed in a hot-wall quartz tube under atmospheric pressure. The etching gas was HCl (> 99.999% purity). N_2 (dew point <−110 °C) was used as the carrier gas. Two series of etching experiments were carried out. The first series of experiments was performed at T = 548–949 °C with P_0(HCl) = 62.5 Pa. The second series of experiments was performed with P_0(HCl) = 25–250 Pa at T = 750 °C. Each etching time was set so that the depth of the etched depression was similar to those of the other samples assuming linear dependence of the etching rate on T or P_0(HCl), although there was variation of the depth to some degree in reality.

A surface profiler was used to measure the depth of the etched depression formed at a square opening to calculate the (001) etching rate. Field-emission scanning electron microscopy (SEM) was performed to observe the in-plane and cross-sectional profiles of

the etched structures. For the plan-view observations, a high acceleration voltage of 10 kV was used to observe the profile through the SiO_2 mask. For the cross-sectional observations, the etched trenches were cut with the (010) plane by Ga-focused ion milling. Secondary-ion mass spectrometry (SIMS) was performed to estimate the diffusion of impurities from the mask or etching environment into the β-Ga_2O_3 surface, which needs to be suppressed for fabrication of practical power devices.

The (001) etching rate as a function of T at P_0(HCl) = 62.5 Pa is shown in Fig. 1(a). The etching rate monotonically increased with increasing temperature. The etching rate as a function of P_0(HCl) at T = 750 °C is shown in Fig. 1(b). The etching rate linearly increased with increasing P_0(HCl).

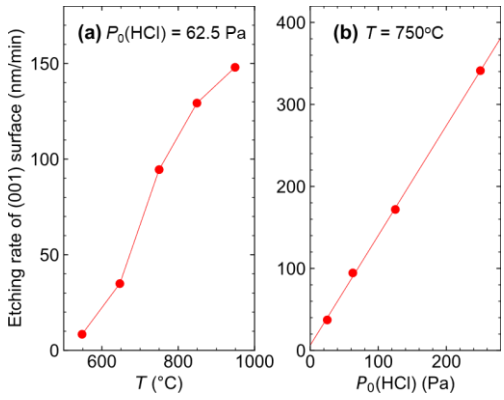

Fig. 1. Etching rate of (001) β-Ga_2O_3 as a function of (a) T at P_0(HCl) = 62.5 Pa and (b) P_0(HCl) at T = 750 °C.

Plan-view SEM images of the etched depressions formed through the circular windows at various T and P_0(HCl) values are shown in Fig. 2(a) and (b). The depressions were nearly hexagonal with sidewalls of {100} and {310}. In both series, the shapes of the upper half of the hexagons, which consisted of the edges of $(\bar{1}00)$, $(\bar{3}\bar{1}0)$, and $(\bar{3}10)$, were similar, while those of the lower part were dependent on the etching conditions. The relative etching rate along [100] to $[\bar{1}00]$ increased with decreasing T and increasing P_0(HCl), and the relative lengths of the edges of $(3\bar{1}0)$ and (310) increased as a result. The anisotropic behavior between [100] and $[\bar{1}00]$ is interesting because they should be crystallographically equivalent. The side wall on the [100] side (+a sidewall) was the stable (100) plane, while that on the $[\bar{1}00]$ side (–a sidewall) deviated from the (100) plane, particularly at low T or high P_0(HCl) (Fig. 3). Furthermore, the –a sidewall stayed just below the window, through which HCl gas was supplied, while the +a sidewall was distant from the window, except for in the initial stage of etching. These results seem to indicate that the –a sidewall had a faster etching rate than the +a sidewall, but the reality was the opposite. The different etching behavior of the ±a sidewalls might be attributable to their cross-sectional geometric differences or the different etching histories starting from the initial horizontal (001) plane to reach the differently inclined ±a sidewalls. However, we do not have any plausible explanation of the concrete mechanism at present.

It is also likely that there was some difference in the microscopic surface structures between these sidewalls. In addition, bowing of the +*a* sidewall was observed when it was distant from the window. This bowing probably occurred because the etching driving force decreased when the etching front was away from the circular window, through which HCl gas was supplied. Accordingly, longer etching time may lead to bending of other sidewalls.

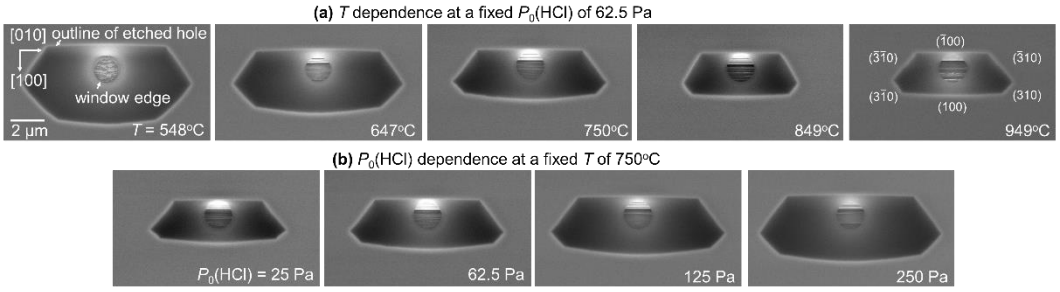

Fig. 2. Plan-view SEM images of the etched depressions formed through circular windows for the (a) *T* series and (b) P_0(HCl) series.

Here, we discuss the cross-sectional shapes of the trenches etched through the striped windows, which are particularly important for fabrication of fins/trenches. Plan-view SEM images of the trenches are shown in Fig. S1. Bowing of the [010]-parallel sidewalls was not observed since the supply and exhaust of the etching-related gas species should be spatially uniform, unlike the case of circular windows. Cross-sectional SEM images of the trenches formed at various *T* and P_0(HCl) values are shown in Fig. 3(a) and (b). A

focused-ion-beam SEM combined apparatus was used for sample preparation and observation. The carbon protective layer deposited for Ga-focused ion milling can be observed. The sidewalls of the trench were parallel or close to the (100) plane, and the bottom was the (001) plane. The inclined ($\bar{1}01$) plane only appeared at the bottom corner on the +*a* sidewall side at T = 949 °C. At T = 1038 °C, the trench bottom was the ($\bar{1}01$) plane without the (001) plane.[29] These results indicate that the ($\bar{1}01$) plane is more stable than the (001) plane at high T. As observed for the circular windows, the etching rate of the +*a* sidewalls was faster than that of the –*a* sidewalls. The structural parameters of the trenches, which are defined in Fig. 3(c), are summarized in Fig. 4. The –*a* sidewall angle θ_{-a} increased with decreasing T and increasing P_0(HCl), while θ_{+a} virtually remained constant. The deviation of θ_{+a} from β = 103.7° is probably due to the geometric error upon tilted observation. The reason for the variation of θ_{-a} is unclear at present. The mechanism may be related to that of the etching rate difference between the ±*a*-sidewalls. In addition, low cross-sectional aspect ratios L_{+a}/D and L_{-a}/D, which are preferable for fabrication of narrow/deep structures, can be obtained at high T or low P_0(HCl), as shown in Fig. 4.

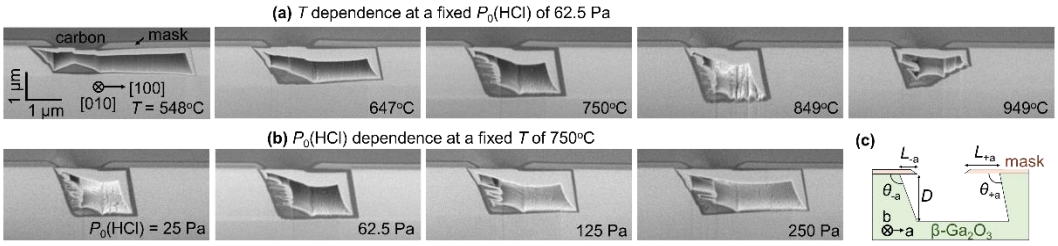

Fig. 3. Cross-sectional SEM images of the etched trenches for the (a) T series and (b) P_0(HCl) series observed from the direction tilted from the (001) surface normal by 54°. (c) Definitions of the measured lengths and angles shown in Fig. 4.

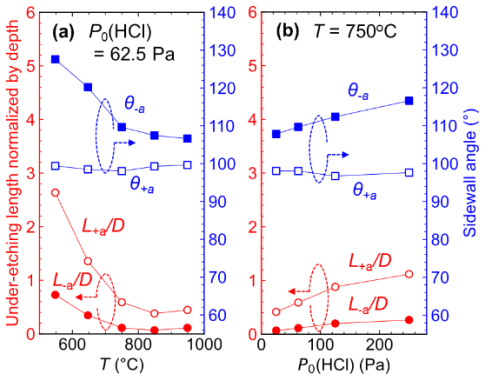

Fig. 4. Normalized under-etching lengths and side-wall angles as a function of (a) T and (b) P_0(HCl). See Fig. 3(c) for the definitions of L_{+a}, L_{-a}, θ_{+a}, θ_{-a}, and D.

The SIMS depth profiles of the (001) β-Ga_2O_3 substrates, including the control sample, are shown in Fig. 5(a)–(c). The measurement was performed on the (001) surface from which the SiO_2 mask was removed by buffered HF etching in advance. The control sample only experienced SiO_2 deposition and removal. No significant morphological difference was observed between the three samples by AFM in the vicinity of the SIMS spots (not shown). The H, Si, and Cl concentrations were measured, and only Si was

detected. The Si depth profiles are compared in Fig. 5(d). Si diffusion, probably from the mask, was observed in the vicinity of the surface for the 949 °C sample, while there was no difference between the 750 °C-annealed and control samples.

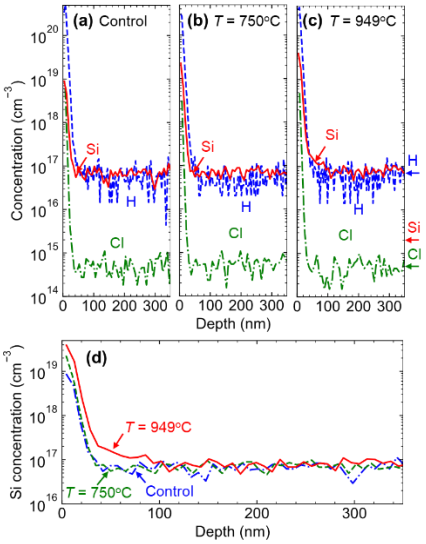

Fig. 5. SIMS depth profiles of the (a) control sample and the samples etched at (b) T = 750 °C and (c) 949 °C. (d) Comparison of the Si concentrations in the three samples. The detection limits are indicated by the arrows.

The behavior of selective-area HCl-gas etching of (001) β-Ga_2O_3 single-crystal substrates has been systematically investigated with T and P_0(HCl) as the parameters. The (001) etching rate monotonically increased with increasing T and P_0(HCl). The relative etching rate of the +a sidewalls to the –a sidewalls increased at low T/high P_0(HCl). The cross-sectional aspect ratios L_{+a}/D and L_{-a}/D of the [010] trenches tended to be small at high T/low P_0(HCl). As guidelines for fabrication of fins/trenches, etching with high T below 949 °C and low P_0(HCl) should be performed to minimize the L/D values and the

deviation of θ_{-a} from β = 103.7° for precise shape/dimension control and negligible Si diffusion.

Acknowledgment

Preparation of the masks and observation of the etched structures were performed at the nanofabrication open facilities of the National Institute for Materials Science (23NM5073).

References

1) M. Orita, H. Ohta, and M. Hirano, H. Hosono, Appl. Phys. Lett. **77**, 4166 (2000).
2) T. Onuma, S. Saito, K. Sasaki, T. Masui, T. Yamaguchi, T. Honda and M. Higashiwaki, Jpn. J. Appl. Phys. 54 112601 (2015).
3) H. Aida, K. Nishiguchi, H. Takeda, N. Aota, K. Sunakawa, and Y. Yaguchi, Jpn. J. Appl. Phys. **47**, 8506–8509 (2008).
4) A. Kuramata, K. Koshi, S. Watanabe and Y. Yamaoka: Galium oxide -Materials Properties, Crystal Growth, and Devices, Ed. By M. Higashiwaki and S. Fujita, Chapter 4 (Springer, 2020).
5) K. Hoshikawa, T. Kobayashi, Y. Matsuki, E. Ohba, T. Kobayashi: J. Cryst. Growth

545, 125724 (2020).

6) K. Hoshikawa, T. Kobayashi, E. Ohba, T. Kobayashi.: J. Cryst. Growth **546**, 125778 (2020).

7) Y. Ueda, T. Igarashi, K. Koshi, S. Yamakoshi, K. Sasaki and A. Kuramata: Jpn. J. Appl. Phys. **62**, SF1006 (2023).

8) Z. Galazka: J. Appl. Phys. **131**, 031103 (2022).

9) J. D. Blevins, K. Stevens, A. Lindsey, G. Foundos, and L. Sande: IEEE TRANSACTIONS ON SEMICONDUCTOR MANUFACTURING **32**, 466 (2019).

10) T. Oshima, T. Okuno, N. Arai, N. Suzuki, S. Ohira, and S. Fujita, Appl. Phys. Express **1**, 011202 (2008).

11) P. Dong, J. Zhang, Q. Yan, Z. Liu, P. Ma, H. Zhou, and Y. Hao, IEEE Electron Device Lett. **43**, 765 (2022).

12) K. Sasaki, D. Wakimoto, Q. T. Thieu, Y. Koishikawa, A. Kuramata, M. Higashiwaki, and S. Yamakoshi, IEEE Electron Device Lett. **38**, 783 (2017).

13) F. Otsuka, H. Miyamoto, A. Takatsuka, S. Kunori, K. Sasaki, and A. Kuramata, Appl. Phys. Express **15**, 016501 (2022).

14) T. Oshima, Y. Kato, N. Kawano, A. Kuramata, S. Yamakoshi, S. Fujita, T. Oishi, and M. Kasu, Appl. Phys. Express **10**, 035701 (2017).

15) A. Vaidya, C. N. Saha, and U. Singisetti, IEEE Electron Device Lett. **42**, 1444 (2021).

16) M. Higashiwaki, K. Sasaki, T. Kamimura, M. Hoi Wong, D. Krishnamurthy, A. Kuramata, T. Masui, and S. Yamakoshi, Appl. Phys. Lett. **103**, 123511 (2013).

17) K. Zeng, R. Soman, Z. Bian, S. Jeong, and S. Chowdhury, IEEE Electron Device Lett. **43**, 1527 (2022).

18) K. D. Chabak, N. Moser, A. J. Green, D. E. Walker, S. E. Tetlak, E. Heller, A. Crespo, R. Fitch, J. P. McCandless, K. Leedy, M. Baldini, G. Wagner, Z. Galazka, X. Li, and G. Jessen, Appl. Phys. Lett. **109**, 213501 (2016).

19) W. Li, K. Nomoto, Z. Hu, T. Nakamura, D. Jena, and H. G. Xing, in IEEE International Electron Devices Meeting (IEEE, 2019), pp. 12.4.1–12.4.4.

20) H. Huang, Z. Ren, AFM A. U. Bhuiyan, Z. Feng, Z. Yang, X. Luo, A. Q. Huang, A. Green, K. Chabak, H. Zhao, and X. Li, Appl. Phys. Lett. **121**, 052102 (2022).

21) R. Khanna, K. Bevlin, D. Geerpuram, J. Yang, F. Ren, and S. Pearton, Gallium Oxide (Elsevier, 2019), pp. 263–285.

22) W. Li, K. Nomoto, Z. Hu, D. Jena, and H. G. Xing, IEEE Electron Device Lett. **41**, 107 (2020).

23) Z. Hu, K. Nomoto, W. Li, Z. Zhang, N. Tanen, Q. T. Thieu, K. Sasaki, A. Kuramata, T. Nakamura, D. Jena, and H. G. Xing, Appl. Phys. Lett. **113**, 122103 (2018).

24) K. D. Chabak, N. Moser, A. J. Green, D. E. Walker, S. E. Tetlak, E. Heller, A. Crespo, R. Fitch, J. P. McCandless, K. Leedy, M. Baldini, G. Wagner, Z. Galazka, X. Li, and G. Jessen, Appl. Phys. Lett. **109**, 213501 (2016).

25) Y. Oshima, E. Ahmadi, S. Kaun, F. Wu and J. S. Speck, Semicond. Sci. Technol. **33**, 015013 (2018).

26) N. K. Kalaricka, A. Fiedler, S. Dhara, H. Huang, A F M A. U. Bhuiyan, M. W. Rahman, T. Kim, Z. Xia, Z. J. Eddine, A. Dheenan, M. Brenner, H. Zhao, J. Hwang, and S. Rajan, Appl. Phys. Lett. **119**, 123503 (2021).

27) H. Huang, M. Kim, X. Zhan, K. Chabak, J. D. Kim, A. Kvit, D. Liu, Z. Ma, J. Zuo, and X. Li, ACS Nano **13**, 8784 (2019).

28) Y. Yamazaki, M. Tomoaki, A. Takeki, and A. Kikuchi, in 4th International Workshop on Gallium Oxide and Related Materials, 2022.

29) T. Oshima and Y. Oshima, Appl. Phys. Lett. **122**, 162102 (2023).

30) T. Oshima and Y. Oshima, Appl. Phys. Express **15**, 075503 (2022).